Vertical artifacts in high-resolution WorldView-2 and WorldView-3 satellite imagery of aquatic systems

Megan M. Coffer[a,b], **Peter J. Whitman**[a], **Blake A. Schaeffer**[a], **Victoria Hill**[c], **Richard C. Zimmerman**[c], **Wilson B. Salls**[a], **Marie C. Lebrasse**[a,d], **David D. Graybill**[a]

[a]U.S. Environmental Protection Agency, Office of Research and Development, Durham, NC, USA

[b]Center for Geospatial Analytics, North Carolina State University, Raleigh, NC, USA

[c]Department of Ocean & Earth Sciences, Old Dominion University, Norfolk, VA, USA

[d]Department of Marine, Earth and Atmospheric Sciences, North Carolina State University, Raleigh, NC, USA

Abstract

Satellite image artefacts are features that appear in an image but not in the original imaged object and can negatively impact the interpretation of satellite data. Vertical artefacts are linear features oriented in the along-track direction of an image system and can present as either banding or striping; banding are features with a consistent width, and striping are features with inconsistent widths. This study used high-resolution data from DigitalGlobe's (now Maxar) WorldView-3 satellite collected at Lake Okeechobee, Florida (FL), on 30 August 2017. This study investigated the impact of vertical artefacts on both at-sensor radiance and a spectral index for an aquatic target as WorldView-3 was primarily designed as a land sensor. At-sensor radiance measured by six of WorldView-3's eight spectral bands exhibited banding, more specifically referred to as non-uniformity, at a width corresponding to the multispectral detector sub-arrays that comprise the WorldView-3 focal plane. At-sensor radiance measured by the remaining two spectral bands, red and near-infrared (NIR) #1, exhibited striping. Striping in these spectral bands can be attributed to their time delay integration (TDI) settings at the time of image acquisition, which were optimized for land. The impact of vertical striping on a spectral index leveraging the red, red edge, and NIR spectral bands—referred to here as the NIR maximum chlorophyll index (MCI_{NIR})—was investigated. Temporally similar imagery from the European Space Agency's Sentinel-3 and Sentinel-2 satellites were used as baseline references of expected chlorophyll values across Lake Okeechobee as neither Sentinel-3 nor Sentinel-2 imagery showed striping. Striping was highly prominent in the MCI_{NIR} product generated using WorldView-3 imagery, as noise in the at-sensor radiance exceeded any signal of chlorophyll in the image. Adjusting the image acquisition parameters for future tasking of WorldView-3 or the functionally similar WorldView-2 satellite

CONTACT Megan M. Coffer, coffer.megan@epa.gov, U.S. Environmental Protection Agency, Office of Research and Development, Durham, NC, USA.

may alleviate these artefacts. To test this, an additional WorldView-3 image was acquired at Lake Okeechobee, FL, on 26 May 2021 in which the TDI settings and scan line rate were adjusted to improve the signal-to-noise ratio. While some evidence of non-uniformity remained, striping was no longer noticeable in the MCI_{NIR} product. Future image tasking over aquatic targets should employ these updated image acquisition parameters. Since the red and NIR #1 spectral bands are critical for inland and coastal water applications, archived images not collected using these updated settings may be limited in their potential for analysis of aquatic variables that require these two spectral bands to derive

1.   Introduction

Satellite remote sensing can provide improved spatial and temporal coverage and resolution compared to field monitoring (Papenfus et al. 2020; Greb et al. 2018; Palmer, Kutser and Hunter 2015). However, satellite image artefacts, defined as features that appear in an image but not in the original imaged object, can negatively impact image quality and the interpretation of remote sensing data products. Vertical artefacts are linear features oriented in the along-track direction of an imaging system and can occur due to a variety of factors, including sensor engineering, the imaging process, and the subject being imaged. Vertical artefacts can have either a consistent width, defined as banding, or inconsistent widths, defined as striping. Banding and striping can produce visually flawed imagery, and parameters derived from imagery affected by these artefacts can produce erroneous quantitative results. Vertical artefacts are particularly problematic in homogeneous regions (e.g., open water, desert, snow, and ice) and in aquatic environments that present optically dark targets relative to land (Zhao et al. 2013). Vertical artefacts have been documented in imagery from several satellite sensors across varying spatial resolutions, including Aqua and Terra's Moderate Resolution Imaging Spectroradiometer at 250-m to 1-km spatial resolution (Bouali and Ladjal 2011; Rakwatin, Takeuchi and Yasuoka 2007), Landsat 4–5's Thematic Mapper at 30-m spatial resolution (Helder, Quirk and Hood 1992; Barker 1984; Metzler and Malila 1985; Nichol and Vohora 2004), Earth Observing-1's Hyperion hyperspectral imaging instrument, also at 30-m spatial resolution (Zhao et al. 2013), and both GeoEye-1 and WorldView-2 at 1.84-m spatial resolution (Dai and Howat 2018).

Satellite remote sensing has proven to be an effective monitoring tool for aquatic systems and has been used to measure various bio-geophysical parameters, including water clarity (Zhang et al. 2021; Olmanson, Bauer and Brezonik 2008), chlorophyll-*a* (Odermatt et al. 2012), harmful algal blooms (Hansson and Hakansson 2007; Maguire et al. 2016), submerged vegetation (Traganos and Reinartz 2017; Pasqualini et al. 2005), bathymetry (Dekker et al. 2011), sediment (Dogliotti et al. 2015), coloured dissolved organic matter (Brezonik et al. 2015), and surface oils (De Carolis, Adamo and Pasquariello 2013; Kolokoussis and Karathanassi 2018). High spatial resolution sensors are required for satellite remote sensing of inland waters (Hestir et al. 2015; Clark et al. 2017; Mouw et

al. 2015; Lee et al. 2012). Commercial satellite imagery has been encouraged as an option to improve spatial resolution in aquatic systems (Schaeffer and Myer 2020; Dekker and Hestir 2012), and has been employed in recent studies for aquatic applications (Coffer et al. 2020; Mishra, Stumpf and Meredith 2019; Wang, Gong and Pu 2018; El Saadi, Yousry and Jahin 2014). However, an investigation into the radiometric quality of commercial satellite imagery, particularly regarding vertical artefacts, is still needed.

To address this paucity in the literature, our study used data from WorldView-3, one of DigitalGlobe's (now Maxar) commercial satellite platforms, as a demonstration, with data from the European Space Agency's (ESA) Copernicus Sentinel-3 and Sentinel-2 satellites used as baseline references. At-sensor radiance for each of WorldView-3's eight spectral bands was considered as well as a spectral index leveraging the red, red edge, and near-infrared (NIR) spectral bands. This spectral index is referred to here as the NIR maximum chlorophyll index (MCI_{NIR}) to emphasize the use of the NIR spectral band rather than the red edge spectral band used in the original definition of MCI as WorldView-2 lacks an equivalent spectral band (Gower et al. 2005). Chlorophyll is an algal pigment whose abundance is used to estimate water quality response to ecosystem stress and to categorize trophic state in aquatic environments. While all digital images are subject to some influence from vertical artefacts, this analysis aimed to determine if the vertical artefacts present in WorldView-3 images prevented realistic characterization of water quality parameters. The following research objectives were addressed:

1. Investigate the sources of vertical artefacts, including both banding and striping, in each spectral band of WorldView-3 imagery.

2. Quantify the influence of vertical artefacts on both at-sensor radiance and satellite-derived MCI_{NIR} values.

3. Optimize WorldView-2 and WorldView-3 image acquisition parameters for aquatic targets to alleviate vertical artefacts.

2. Materials and methods

2.1. Study site

Lake Okeechobee in Florida (FL; 26.97°N, 80.80°W), USA, is the largest lake in the state and the fifth largest lake in the country by surface area, excluding the Great Lakes (Figure 1). Lake Okeechobee was chosen for this study because of its large surface area, which provided ample opportunity to evaluate pure water pixels. Large lakes reduce the potential of stray light contamination from land which can negatively impact data quality (Palmer, Kutser and Hunter 2015), a concern for both the WorldView-3 imagery and the coarser resolution Sentinel-3 and Sentinel-2 imagery. Additionally, Lake Okeechobee experiences frequent algal blooms (Rosen et al. 2017), which is an important consideration for this study given the use of MCI_{NIR}, a spectral index that quantifies chlorophyll concentration. Although vertical artefacts have been visually confirmed in many WorldView-2 and WorldView-3 scenes (results not shown), a single-case study using WorldView-3 data at Lake Okeechobee was chosen here as a quantitative demonstration.

2.2. Satellite data

Satellite imagery was acquired from Maxarʻs WorldView-3 satellite, while imagery from ESAʻs Sentinel-3 and Sentinel-2 satellites was used as baseline references. Image acquisition dates for each satellite image are shown in Table 1. A flowchart outlining specific image processing steps applied to WorldView-3 (Section 2.2.1), Sentinel-3 (Section 2.2.2), and Sentinel-2 (Section 2.2.3) imagery is shown in Figure 2.

2.2.1.   WorldView-3—DigitalGlobe launched WorldView-3 in August 2014 (Maxar 2019). WorldView-3 is a pushbroom sensor offering multispectral data at 1.24-m spatial resolution at nadir and 1.38-m spatial resolution at 20° off-nadir. While vertical artefacts are also present in imagery from Maxarʻs WorldView-2 satellite sensor, only WorldView-3 is shown here. Both the WorldView-2 and the WorldView-3 satellite sensors utilize time delay integration (TDI) charge-coupled devices (CCD) for image capture. In TDI line scan imaging, images are taken continuously while the sensor moves in a straight line at constant velocity. Light from a single target is imaged onto a single pixel, and as the sensor moves, the light read for that single pixel is transferred to the pixel below it at the same velocity at which the sensor is moving. The light captured from the single target is then summed across the number of pixels corresponding to the TDI settings for that spectral band, similar to a moving window; for a TDI setting of 10, for example, 10 pixels are activated and their measured values are summed to generate a single value, which is assigned to a single pixel. The scan line rate at the time of image acquisition indicates the number of lines the CCD scans per second. TDI CCD's are commonly used for capturing fast-moving targets in low-light conditions because it allows additional incident light to be included in the at-sensor radiance measured for each satellite pixel (Chamberlain and Washkurak 1990).

Three basic level 1B WorldView-3 images, collected on 30 August 2017, were obtained from DigitalGlobeʻs EnhancedView Web Hosting Service (evwhs.digitalglobe.com). These images were selected as they had full coverage of Lake Okeechobee with minimal cloud interference. WorldView-3ʻs default image acquisition parameters were used, which are optimized for land and included TDI settings for each spectral band ranging from 10 to 24 and a scan line rate of 20,000 lines per second. Limited processing was applied to WorldView-3 data to ensure results presented here characterized the imagery itself and not the selected processing regime. Metadata associated with basic level 1B imagery was adjusted using updated vicarious calibration factors provided by Kuester (2017). Relative radiometric calibration is provided with basic level 1B data, and absolute radiometric calibration was performed following Coffer et al. (2020) to convert digital numbers to top-of-atmosphere radiance (L_{TOA}) in units of Watts per steradian per square meter ($Wsr^{-1}m^{-2}$). Tiles contained in each of the three scenes were mosaicked together and clipped to the boundary of Lake Okeechobee. For comparison to Sentinel-2 imagery, MCI_{NIR} derived from WorldView-3 imagery was downsampled to match the 20-m spatial resolution of Sentinel-2 via bilinear interpolation.

As suggested in Section 3.1, vertical artefacts in the WorldView-3 images collected on 30 August 2017 could be partly attributed to the use of default image acquisition parameters, which are optimized for land. To test if adjusting these acquisition parameters alleviated

vertical artefacts, an additional WorldView-3 image consisting of a single image tile was collected over Lake Okeechobee, FL, on 26 May 2021 using parameters optimized for aquatic targets, which involved increasing the TDI rate to 24 for all spectral bands and decreasing the scan line rate to 12,000 lines per second. As with the 30 August 2017 data, the 26 May 2021 data were obtained as basic level 1B data, relative and absolute radiometric calibration were applied, and the image was clipped to the boundary of Lake Okeechobee. WorldView-3 image processing was performed in ENVI 8.7.0 and IDL 8.7.2 (Exelis Visual Information Solutions, Boulder, Colorado). Image mosaicking, clipping, and downsampling were performed in ArcGIS Version 10.7.1 (ESRI 2019).

2.2.2.   Sentinel-3—While Sentinel-3 imagery has insufficient spatial resolution (300-m at nadir) to directly compare to high spatial resolution satellite platforms such as WorldView-3, its frequent temporal resolution (near-daily) can allow for contemporaneous data collection. Temporally coincident Sentinel-3 imagery was used here to provide information regarding algal blooms in Lake Okeechobee at the time of WorldView-3 image collection. ESA launched the Copernicus Sentinel-3A satellite in February 2016 and the Copernicus Sentinel-3B satellite in April 2018, hereafter collectively referred to as Sentinel-3. Each satellite is equipped with the Ocean and Land Colour Instrument (OLCI). OLCI collects data in multiple spectral bands spanning the red and red edge portions of the electromagnetic spectrum, a region crucial for measuring chlorophyll. Here, the cyanobacteria index (CI-cyano), which leverages reflectances from OLCI between 620 and 709 nm to estimate cyanobacteria abundance (Lunetta et al. 2015; Wynne et al. 2008, 2010), was used as evidence of algal blooms across Lake Okeechobee. OLCI imagery was first collected by ESA through the Copernicus program and was then processed into CI-cyano by the National Aeronautics and Space Administration (NASA) Ocean Biology Processing Group (https://oceancolor/gsfc.nasa.gov/projects/cyan/). Two Sentinel-3 images were obtained for comparison to WorldView-3 imagery; one was obtained for 31 August 2017, 1 day after the 30 August 2017 WorldView-3 image acquisition, and another was obtained for 26 May 2021, the same day as the 26 May 2021 WorldView-3 image acquisition.

2.2.3.   Sentinel-2—Vertical artefacts were investigated in imagery from WorldView-3 while imagery from Sentinel-2 was used as a baseline reference. All digital images, including those from Sentinel-2, are affected in some way by vertical artefacts (Warren et al. 2019); however, previous studies applying spectral indices to Sentinel-2 imagery have demonstrated that vertical artefacts did not hinder quantification of water quality parameters (Toming et al. 2016; Oiry and Barillé 2021) as the error introduced through vertical artefacts did not outweigh the signal of the attribute being measured. Thus, Sentinel-2 imagery was used as a baseline reference to compare satellite-derived chlorophyll concentrations across Lake Okeechobee against results from WorldView-3.

Temporally and spatially coincident scenes between WorldView-3 and Sentinel-2 were desired in order to quantify the additional variability introduced as a result of vertical artefacts in WorldView-3 imagery. However, there were no Sentinel-2 scenes coincident with scenes from WorldView-2 or WorldView-3 due to the infrequent and intermittent temporal

coverage of commercial satellite imagery. Therefore, Sentinel-2 was used to develop a baseline of expected data variability throughout Lake Okeechobee from the period around the date of the WorldView-3 image collection. Despite the lack of temporal matches between the two datasets, a comparison between WorldView-3 and Sentinel-2 imagery is still valid as Sentinel-2 imagery can capture the expected natural spatial patterns in chlorophyll (Seuront et al. 1996; Mandelbrot 1983) across Lake Okeechobee, whereas WorldView-3 imagery contaminated with vertical artefacts will likely not produce expected natural spatial patterns. In the absence of field-observed chlorophyll, analyzing expected natural spatial patterns can offer insight regarding the reliability of satellite-derived MCI_{NIR} values. For comparison against either WorldView-2 or WorldView-3 data, imagery from Planet Lab‛s RapidEye satellite constellation and the joint NASA and United States Geological Survey (USGS) Landsat series were also considered. However, no coincident scenes between either WorldView-2 or WorldView-3 and RapidEye were available, and Landsat products do not contain the red edge spectral band required to compute MCI_{NIR}. Thus, Sentinel-2 imagery, despite no temporal overlap, was chosen for comparison.

ESA launched the Copernicus Sentinel-2A satellite in June 2015 and the Copernicus Sentinel-2B satellite in March 2017, hereafter collectively referred to as Sentinel-2. Each satellite is equipped with the MultiSpectral Instrument (MSI), which collects multispectral imagery at spatial resolutions of 10, 20, and 60 m at nadir. Sentinel-2 level 1C data were requested as top-of-atmosphere reflectance (R_{TOA}) for the months of August and September 2017 as this time period characterized a one-month period before and after the WorldView-3 image acquisition. Four Sentinel-2 scenes fit these criteria and were selected for analysis. R_{TOA} values were converted to L_{TOA} to match the units of the WorldView-3 data. Cloud masking provided with Sentinel-2 imagery was applied, and satellite tiles for each unique date were mosaicked together and clipped to the boundary of Lake Okeechobee. The red and NIR spectral bands were resampled from their native spatial resolution of 10 m to 20 m to match the spatial resolution of the other multispectral band used in the MCI_{NIR} calculation. MCI_{NIR} was computed as described in Section 2.3. MCI_{NIR} values derived from each of the four Sentinel-2 images were retained for comparison to WorldView-3, and a temporal composite was generated reflecting average MCI_{NIR} across all four images. Sentinel-2 data processing was performed using Google Earth Engine (Gorelick et al. 2017).

2.3.   Spectral index

Since vertical artefacts are particularly visible in relatively homogeneous regions, including water, a variation on a spectral index commonly used in aquatic environments was chosen to assess the influence of vertical artefacts on a derived variable and was adapted to the spectral characteristics of the WorldView-3 and Sentinel-2 sensors (Table 2). MCI is a line height algorithm originally developed by Gower et al. (2005) for imagery from the MEdium Resolution Imaging Spectrometer (MERIS) onboard ESA‛s Envisat satellite. MCI leverages three spectral bands to estimate the chlorophyll concentration: two outer bands used to establish a baseline and one central band use to measure the peak from the baseline. MCI has shown promise when applied to other satellite platforms, including for RapidEye (Mishra, Stumpf and Meredith 2019) and Sentinel-2 (Xu et al. 2019; Ansper and Alikas 2019; Pirasteh et al. 2020). The WorldView-3 and Sentinel-2 satellites are

spectrally different from MERIS; however, this study is not intended to validate the MCI algorithm originally presented in Gower et al. (2005) for additional satellite platforms, but rather to serve as an example of a spectral index using spectral bands relevant for water quality monitoring. Here, MCI was modified to meet the spectral characteristics of WorldView-3 and Sentinel-2 and is referred to as MCI_{NIR}, leveraging radiances in the red and NIR spectral bands as the two outer bands in the MCI_{NIR} equation, and the red edge spectral band as the peak band to estimate the relative chlorophyll abundance (Equation 1). MCI_{NIR} was retained as a relative index and was not converted to an absolute chlorophyll concentration. MCI_{NIR} was computed as:

$$MCI_{NIR} = L_{TOA}(\lambda_{red\,edge}) - L_{TOA}(\lambda_{red}) \times$$
$$\left[\frac{\lambda_{red\,edge} - \lambda_{red}}{\lambda_{NIR} - \lambda_{red}} \times L_{TOA}(\lambda_{NIR}) - L_{TOA}(\lambda_{red}) \right] \tag{1}$$

2.4. Quantifying vertical artefacts in at-sensor radiance

Using a single image tile, at-sensor radiance measured by each of WorldView-3's eight spectral bands was first used to characterize the width of vertical artefacts for each spectral band. Next, at-sensor radiance values were extracted across a horizontal transect to investigate the influence of vertical artefacts on the resulting radiance values. For each spectral band, the mean and standard deviation of all data values across the horizontal transect were computed. Standard deviations for all eight spectral bands were analysed for outliers. Mild and extreme outliers were defined by Barbato et al. (2011) using the inner fence and outer fence of the distribution. The inner fence is defined as the first quartile minus 1.5 times the interquartile range and the third quartileplus 1.5 times the interquartile range. The outer fence is defined as the first quartile minus 3 times the interquartile range and the third quartile plus 3 times the interquartile range. A point beyond an inner fence on either side is considered a mild outlier, while a point beyond an outer fence on either side is considered an extreme outlier.

2.5. Quantifying vertical artefacts in satellite-derived MCI_{NIR} values

Vertical and horizontal transects across satellite-derived MCI_{NIR} values were compared to quantify noise introduced as a result of vertical artefacts. Three vertical and three horizontal transects were extracted from satellite-derived MCI_{NIR} values in a single WorldView-3 image tile. First, the shape of the distribution for each transect was characterized by computing excess kurtosis (Chissom 1970). Excess kurtosis describes the tail shape of the data distribution. In the event of vertical artefacts, distributions associated with vertical transects should be more compact due to the linear nature of the artefacts, while distributions associated with horizontal transects should be more dispersed as both light and dark biases would be captured in each horizontal transect. Distributions that are more concentrated about the mean are described as leptokurtic and generally have a kurtosis value above zero. Distributions that are more dispersed about the mean are described as platykurtic and generally have a kurtosis value below zero. Excess kurtosis was computed using the *e1071* package in R Version 4.0.0 (Meyer et al. 2019; R Core Team 2020).

As further evidence of vertical artefacts, the two-sample Kolmogorov–Smirnov test was used to quantify if distributions within both vertical and horizontal transects were similar. This analysis tested the hypothesis that vertical transects affected by banding or striping would have different distributions from one another due to light and dark biases across the image, while horizontal transects not affected by banding or striping would have similar distributions from one another. The two-sample Kolmogorov–Smirnov test is a nonparametric test that is sensitive to differences in both location and shape of the empirical cumulative distribution functions of the two samples (Kolmogorov 1933; Smirnov 1939). The Kolmogorov–Smirnov test statistic, D, is the largest difference between the two cumulative distribution functions and ranges from 0 to 1. Generally, values below 0.5 and nearing 0 indicate the two samples were drawn from the same population, suggesting small differences between samples. Values above 0.5 and nearing 1 indicate the two samples were drawn from different populations, suggesting large differences between samples. A p-value is provided with results of the Kolmogorov–Smirnov test, but it is not reported here. While p-values are often included because of their familiarity to many readers, they provide negligible information on the validity of the reported model (Wasserstein, Schirm and Lazar 2019) and can be artificially deflated with large sample sizes (Lantz 2013). The Kolmogorov–Smirnov test was applied using R Version 4.0.0 (R Core Team 2020).

3. Results

3.1. Sources of vertical artefacts in WorldView-3 imagery

Visual inspection of radiance values for each of WorldView-3's eight spectral bands suggests that at least two types of vertical artefacts are occurring in the imagery (Figure 3). Consistent, vertical banding appears to contaminate radiance measured by all spectral bands, although this artefact is most obvious in the coastal blue, blue, green, yellow, red edge, and NIR #2 spectral bands. These banding features are approximately 600 pixels in width, which corresponds to each of the 12 multispectral detector sub-arrays that make up the WorldView-2 and WorldView-3 focal planes (Updike and Comp 2010). Documentation accompanying WorldView-3 imagery notes that 'vertical streaks' may be apparent in the raw imagery resulting from differences in gain or offset values for a single detector, which they refer to as non-uniformity (Updike and Comp 2010; Kuester 2017). The documentation also notes that these artefacts are minimized after relative radiometric correction, which is included in level 1B data. Non-uniformity has been reported in other satellite sensors including in imagery from NASA/USGS's Landsat 8 (Pahlevan et al. 2017b), ESA's Sentinel-2 mission (Pahlevan et al. 2017a), Maxar's WorldView-1 satellite (Krause 2008), Planet Lab's RapidEye satellite constellation (Anderson et al. 2011), and more generally for short-wavelength infrared pushbroom hyperspectral sensors (Hu et al. 2017).

Narrow, inconsistent striping appears in several spectral bands, but most prominently in the red and NIR #1, resulting in highly contrasting and unpredictable light and dark biases in radiance values. The locations of these light and dark biases are similar across the two spectral bands with a wide bright bias in the left half of the tile while the right half of the tile is characterized by dark biases. Striping in red and NIR #1 spectral bands can be attributed to their TDI settings. Image capture utilizing TDI is ideal for capturing

fast-moving objects while preserving light sensitivity (Chamberlain and Washkurak 1990) and is described in detail in Bodenstorfer et al. (2007). Higher TDI settings are preferred in low-light conditions or for low-light targets to allow additional incident light to be included in the at-sensor radiance measured for each pixel (El-Desouki and Al-Azem 2014). Due to hardware limitations, the WorldView-3 satellite is constructed such that the same TDI setting is shared between the coastal blue and NIR #2 spectral bands, the blue and green spectral bands, the yellow and red edge spectral bands, and the red and NIR #1 spectral bands (Updike and Comp 2010). In the image used here, the TDI setting for the red and NIR #1 spectral bands were set to a lower value (TDI = 10) than those of the other three pairs (TDI = 24, 14, and 24, respectively). Red through NIR radiances are generally higher over most land targets due to higher reflectances from vegetation, so it is reasonable for TDI settings to be lower over land for these spectral bands. However, this assumption does not hold over aquatic targets as radiance measured over water in near-infrared wavelengths is much lower, nearing zero. Thus, the lower TDI setting in the red and NIR #1 spectral bands likely led to insufficient signal-to-noise ratio (SNR) to capture an optically dark target, resulting in arbitrary bright and dark striping across the image. A high SNR is essential for measuring constituents in aquatic systems due to the already low signal of water; an insufficient SNR can cause variability in the measured constituent to be concealed by noise within the image (Gordon and Clark 1981).

3.2. Effect of vertical artefacts on radiance values

While the coastal blue, blue, green, yellow, red edge, and NIR #2 spectral bands exhibited visible light and dark biases in their radiance values as a result of non-uniformity (see Figure 3), the extracted data showed little variability in these spectral bands, with standard deviations below 0.001 for each spectral band (Figure 4; Table 3). Radiance values for the red and NIR #1 spectral bands, however, were strongly affected by striping as shown by high variability in extracted radiance values, particularly values in the NIR #1 spectral band (Figure 4). Consequently, the standard deviations of radiance values for the red and NIR #1 spectral bands were considerably higher than for the other six spectral bands. The standard deviation in the red spectral band was two to four times higher than those spectral bands impacted only by banding, and for the NIR #1, the standard deviation was five to ten times higher. Based on the definitions of mild and extreme outliers presented in Barbato et al. (2011), the red spectral band contains mild outliers ($\sigma > 0.0014$), and the NIR #1 spectral band contains extreme outliers ($\sigma > 0.0021$).

3.3. Effect of vertical artefacts on MCI$_{NIR}$ values

Vertical artefacts in WorldView-3's spectral bands resulted in drastically different distributions of MCI$_{NIR}$ values across vertical and horizontal transects (Figure 5). Across vertical transects, the distributions were leptokurtic (excess kurtosis spanned 0.02 to 0.17), meaning the data values were more concentrated about the mean. Each of the three vertical transects had distributions spanning a small range of MCI$_{NIR}$ values (interquartile ranges all equalled 0.00065), and none of the interquartile ranges overlapped. The three horizontal transects had distributions that can be described as platykurtic (excess kurtosis spanned −0.87 to −0.59), meaning their data values were more dispersed about the mean. The values within the interquartile ranges for the horizontal transects were much more similar (spanning

0.00298 to 0.00561), with each median falling within the interquartile ranges of the other two distributions.

Results of the two-sample Kolmogorov–Smirnov test also supported differences in the vertical transect distributions and similarities in the horizontal transect distributions (Table 4). Between each possible pairing of vertical distributions, the Kolmogorov–Smirnov test statistic indicated a large difference between samples (D = 1.00, 0.99, and 1.00), suggesting derived MCI_{NIR} values from different vertical transects are not from the same population. Between each possible pairing of horizontal distributions, the Kolmogorov–Smirnov test statistic indicated a small difference between samples (D = 0.07, 0.37, and 0.34). This offers quantitative evidence of the stark contrast in data values imposed by vertical artefacts in the imagery, which can cause large variability in derived geophysical variables.

Erroneous MCI_{NIR} values derived from WorldView-3 are evident across all of Lake Okeechobee, while results derived from Sentinel-2 indicate a much more reasonable pattern of data values (Figure 6). Radiance measured from these WorldView-3 and Sentinel-2 scenes have not been cross-calibrated, meaning resulting MCI_{NIR} values derived from each sensor cannot be directly compared (Pancorbo et al. 2021); however, visually comparing results between sensors can offer evidence of errors introduced as a result of vertical artefacts in WorldView-3 imagery. MCI_{NIR} derived from WorldView-3 imagery showed sharp changes in data values with vertical bands of varying width spanning the entire north–south extent of the lake and extremely high MCI_{NIR} values in a vertical stripe near the center of the lake (Figure 6(a)). The Sentinel-2 composite, however, showed no increased chlorophyll activity in this region. Instead, according to the Sentinel-2 composite, chlorophyll was most concentrated along the northwestern shore of the lake (Figure 6(d)), an area that had very low MCI_{NIR} values in the WorldView-3 image. Sentinel-3 imagery taken the day after the 30 August 2017 WorldView-3 overpass also suggested an algal bloom was present along the northern shore of Lake Okeechobee (Figure 7). A horizontal transect across a subset of the lake using WorldView-3 imagery indicated sudden variations in MCI_{NIR} (Figure 6(c)), while the same transect using both the composite Sentinel-2 data and data from the four individual scenes used to create the composite showed much more gradual changes across the subset (Figure 6(f)). In the WorldView-3 scene, variability in sensor-derived MCI_{NIR} was the result of both variability in the measured geophysical variable itself and artefacts caused by vertical striping; however, the influence of each of these factors cannot be directly quantified without large-scale field observations.

3.4. Minimizing striping in future image acquisitions

Both WorldView-2 and WorldView-3 were designed primarily as land sensors; thus, the default acquisition parameters are optimized for land targets. During future image tasking of WorldView-2 or WorldView-3, acquisition settings should be optimized to properly serve each specific use case. For aquatic applications, for example, adjusting both TDI settings and the scan line rate may help alleviate vertical artefacts, including striping. Increasing the TDI settings and decreasing the scan line rate during image acquisition may increase the SNR of the data. In WorldView-2 and WorldView-3 products, the maximum available TDI

setting for multispectral bands is 24 (Updike and Comp 2010), and the minimum potential scan line rate is 12,000 lines per second compared to its default value of 20,000.

An additional WorldView-3 image was collected over Lake Okeechobee, FL, on 26 May 2021 using image acquisition parameters optimized for aquatic targets, and MCI_{NIR} was computed (Figure 8). Note that the exact same image tile shown in Figure 3 was not used for comparison due to differences in pixel size and swath width between the two scenes as the view angle differed between image acquisitions: the 30 August 2017 image was collected at a view angle of 19.4° and the 26 May 2021 image was collected at a view angle of 37.8°. Both the true colour image and the derived MCI_{NIR} product indicated a chlorophyll event in the southwestern portion of the image tile. Temporally and spatially coincident OLCI imagery also supported the presence of chlorophyll (Figure 9). MCI_{NIR} derived from the WorldView-3 image collected using acquisition parameters optimized for aquatic targets does not appear to be impacted by striping, although some evidence of banding remains. Nevertheless, the increased SNR resulting from adjusted TDI settings and scan line rate allowed for the signal of the attribute being measured, chlorophyll, to outweigh errors introduced through vertical artefacts.

Vertical and horizontal transects were extracted for a subset of the image tile shown in Figure 8 (Figure 10). In the absence of striping in the red and NIR #1 spectral bands, values extracted along vertical and horizontal transects should have similar distributions unlike those shown in Figure 5 For MCI_{NIR} derived from the image collected on 26 May 2021. All vertical and horizontal distributions were leptokurtic (excess kurtosis spanned 0.83 to 26.57), meaning the data values were more concentrated about the mean. Results of the two-sample Kolmogorov–Smirnov test also support more similar distributions for vertical and horizontal transect distributions of MCI_{NIR}. Between each possible pairing of distributions, the Kolmogorov–Smirnov test statistic indicated small differences between samples (Table 5; *D* spanned 0.12 to 0.36). Moreover, visual interpretation would suggest that these differences are the result of differences in the concentration of chlorophyll rather than artificial differences caused by striping.

4. Discussion

Field observations would be required to definitively support algal presence; however, imagery from both Sentinel-2 and Sentinel-3 suggested algae were present in Lake Okeechobee on 31 August 2017, predominantly along the northern shore of the lake. Consequently, the highest MCI_{NIR} values across the scene should highlight pixels that contain algae. Instead, the highest and lowest MCI_{NIR} values correspond to vertical striping across the scene, suggesting the variability in radiance values was higher among striping artefacts than it was for the variable being quantified. Additionally, at the time of image acquisition (12:22 EDT), winds at the study site were out of the east-southeast at around 4 ms^{-1}. Surface waters and their constituents, including cyanobacteria, tend to move in the direction of the wind (Wu et al. 2013). Thus, winds out of the east-southeast would create a diagonal gradient in the algal filaments present in the surface waters at Lake Okeechobee. This should lead to fairly equivalent horizontal and vertical variability, but, instead, horizontal gradients show much more variability across the image (see Figure

5), suggesting that this variability is due to vertical artefacts in the image and not the geophysical variables being estimated. Additionally, the composite Sentinel-2 data suggest that the highest chlorophyll values occurred along the northwest shoreline of Lake Okeechobee, and the Sentinel-3 data suggest that the highest chlorophyll values occurred along the northern shore. However, in the WorldView-3 image, the highest chlorophyll values occur in a vertical stripe near the centre of the lake.

Vertical artefacts can also be explained by bright targets within an image if satellite pixels become saturated. Two image artefacts involving sensor saturation, namely smearing and blooming, have been documented in the literature for satellite imagery and were considered here as potential causes of striping in the red and NIR #1 spectral bands. Smearing occurs when electrons leak into an area of the vertical transfer register, a component of CCD cameras, due to image saturation (Smith et al. 1999). These electrons are then transferred downward causing pixels above and below the saturated area to contain the excess electrons. Smearing manifests as a bright vertical stripe extending above and below the saturated portion of the image. Blooming occurs when pixels in the brightest part of the image lose their ability to accommodate additional electrons, which causes those electrons to spread into neighbouring pixels (Catano 1978). Blooming appears as an isotropic artefact emanating from the saturated pixels and is often also accompanied by vertical streaking in the image. Wahballah, Bazan and Ibrahim (2018) cited smearing in high-resolution satellites, Elvidge et al. (2001) noted blooming in nighttime imagery along coastal areas, and Poli et al. (2015) described artefacts similar to blooming from bright targets in GeoEye-1 and WorldView-2 images. Two anti-blooming techniques, adding a vertical overflow drain (Hamasaki et al. 1988) and a lateral overflow drain (Ando et al. 1991), have been effectively used in other imaging platforms. Neither a vertical nor a lateral overflow drain was implemented in the WorldView-2 sensor design, but WorldView-3 is equipped with a lateral overflow drain (Maxar Technologies Inc., personal communication, 18 June 2021).

There were several WorldView-3 pixels within the entire image strip that reached saturation. These pixels had digital numbers of 2048, which is the maximum possible value that can be achieved in an image with 11-bit radiometric resolution like those collected by WorldView-3. However, the location of these saturated pixels did not correspond to the striping in the red and NIR #1 spectral bands. In the image strip that includes the spatial subset shown in Figure 3, six pixels reached saturation for the red and NIR #1 spectral bands due to specular reflection from buildings located along the northern shore of Lake Okeechobee. Each of the remaining six spectral bands (coastal blue, blue, green, yellow, red edge, and NIR #2) also reached saturation for the same pixel locations and for additional pixel locations (e.g., cloud cover along the southern shore of Lake Okeechobee), but did not show evidence of smearing or blooming. Therefore, sensor saturation was likely not the primarily cause of the striping observed in the red and NIR #1 spectral bands, although it could have contributed.

Striping in the red and NIR #1 spectral bands was likely caused by the TDI settings at the time of image acquisition. According to documentation accompanying WorldView-3 imagery, the TDI settings for each image are selected using a look-up table that considers only the solar elevation angle and does not include any target feature information such as

bright land or dark water, nor does it include a land mask. However, Dai and Howat (2018) noted TDI settings in WorldView-2 and WorldView-3 imagery can pose issues with an improperly defined land mask, as optimal TDI settings differ over land and aquatic targets. Dai and Howat (2018) observed vertical artefacts caused by image saturation over Arctic regions in high-resolution, commercial satellite imagery due to improper TDI settings for the imaged surface. The authors proposed an algorithm for the local detection of vertical artefacts in commercial imagery, but this approach was insufficient for our imagery since: (1) our vertical artefacts occur over optically dark regions rather than optically bright regions, and (2) their algorithm was designed to identify banding in the imagery, whereas the focus of this study is primarily striping.

Striping in the red and NIR #1 spectral bands was no longer evident after adjusting the TDI settings and scan line rate during image capture. It is likely that striping will be particularly prevalent in scenes that capture sharp transitions from optically bright targets, such as land, to optically dark targets, such as water. Algorithms used to assess water quality are typically either empirical or semi-analytical and depend on variations in the spectral shape and magnitude of the water-leaving reflectance (Greb et al. 2018). Erroneous top-of-atmosphere radiance values can be propagated through image processing, resulting in inaccurate derived inherent optical properties and derived water quality parameters. Optimizing these image acquisition parameters for aquatic targets increased the SNR and allowed the chlorophyll signal to exceed noise in the image. Future tasking of both WorldView-2 and WorldView-3 should specify the maximum TDI settings and the minimum scan line rate. Additionally, WorldView-2 can offer slightly higher SNR than WorldView-3 due to its coarser spatial resolution at nadir (1.84 m for WorldView-2 and 1.24 m for WorldView-3), and therefore, could be more appropriate for aquatic applications than WorldView-3. Archived WorldView-2 and WorldView-3 images were likely collected using acquisition parameters optimized for land, meaning they may be inadequate for aquatic applications that require the red and NIR #1 spectral bands.

Vertical artefacts will be particularly problematic when using spectral indices or spectral ratios that utilize spectral bands impacted by striping, such as the red and NIR #1 spectral bands in this study. For a spectral index such as MCI_{NIR}, which utilizes both of these spectral bands as well as the red edge spectral band, vertical artefacts present in each spectral band were compounded; banding in the red edge spectral band and striping in the red and NIR #1 spectral bands resulted in an inconsistent and erroneous display of MCI_{NIR} values across Lake Okeechobee. Spectral indices that do not leverage spectral bands impacted by striping will likely not create such irregular vertical artefacts; this is a focus of ongoing research efforts. Using the RapidEye satellite constellation, Mishra, Stumpf and Meredith (2019) evaluated MCI_{NIR} at Utah Lake, Utah, and did not find evidence of striping in the imagery. Moreover, this artefact is likely less problematic in image classification than in spectral indices as image classification is used to create a categorical product and not a continuous product, thus allowing some errors caused by vertical artefacts to be concealed in the final product. Both Islam et al. (2020) and Coffer et al. (2020) successfully classified seagrass coverage using imagery from WorldView-2 without obvious impacts of vertical artefacts, but additional noise in the red and NIR #1 spectral bands could lead to poorer classification accuracies as pixels of similar classes can become more difficult to distinguish.

This study presents the first analysis of vertical artefacts in commercial satellite imagery for aquatic applications; however, there are several limitations that warrant consideration. Field observations were not available for comparison to satellite-measured radiance or satellite-derived chlorophyll abundance. Therefore, comparisons were made between WorldView-3 and two coarser spatial resolution sensors. Comparing sensors that have not been cross-calibrated can introduce additional, unquantifiable error that is not accounted for here. Obtaining field observations of chlorophyll in order to quantify bias introduced due to vertical artefacts is of interest for both WorldView-2 and WorldView-3 imagery. Moreover, while MCI was originally developed for the MERIS sensor using spectral bands centred at 681, 709, and 753 nm (Gower et al. 2005), this study considered slightly different wavelengths to match the spectral characteristics of the WorldView-3 sensor, which may reduce the ability of the spectral index to properly characterize chlorophyll abundance. There are also spatial and temporal limitations of this study. Only a single WorldView-3 image collected using default image acquisition parameters and a single image collected using updated image acquisition parameters were considered. Future work will expand this demonstration spatially and temporally. And while WorldView-2 was suggested as a potentially more appropriate satellite for aquatic applications due to its coarser spatial resolution and, thus, higher SNR, no WorldView-2 images were tested here. Finally, a sensitivity analysis could refine the updated image acquisition parameters proposed here; iterating through the eight potential TDI rates and scan line rates ranging from 12,000 to 24,000 in increments of 1,000 (Updike and Comp 2010) could offer insight regarding the importance of each parameter on the SNR of each of WorldView-3's eight spectral bands. However, radiometric field measurements would be required for each image acquisition. To test each combination of TDI rates and scan line rates, a minimum of 104 scenes (13 unique scan line rate settings multiplied by 8 unique TDI settings) with coincident field radiometry would be required, which was beyond the scope of this initial study.

5.   Conclusions

This study identified vertical artefacts in WorldView-3 imagery collected over an optically dark and homogeneous region of water. Banding was present in all eight spectral bands, and striping was present in the red and NIR #1 spectral bands. The TDI settings, which were optimized for land targets at the time of image acquisition, were found to cause striping, which led to an inconsistent and erroneous characterization of chlorophyll across Lake Okeechobee. Analyses presented here can be applied to band ratios or other spectral indices used for aquatic applications to characterize potential bias introduced in derived geophysical variables as a result of vertical artefacts. The red and NIR #1 spectral bands are critical for inland and coastal water applications, and striping in these spectral bands can hinder the use of WorldView-2 and WorldView-3 imagery in such environments. For aquatic applications, future tasking of WorldView-2 and WorldView-3 should specify image acquisition parameters suitable for optically dark targets.

Acknowledgements

in the red and NIR #1 spectral bands. DigitalGlobe imagery was made available through the U.S. Government NextView license. This article has been reviewed by the Center for Environmental Measurement and Modeling and approved for publication. Mention of trade names or commercial products does not constitute endorsement or recommendation for use by the U.S. Government. The views expressed in this article are those of the authors and do not necessarily reflect the views or policies of the U.S. EPA.

References

Anderson C, Naughton D, Brunn A, and Thiele M 2011. "Radiometric Correction of RapidEye Imagery Using the on-Orbit Side-Slither Method." In: Image and Signal Processing for Remote Sensing XVII, International Society for Optics and Photonics, 818008.

Ando H, Nakai M, Akimoto H, Ono H, Ozawa N, Ohba S, Suzuki T, Uehara M, and Hikiba M 1991. "A 1/2-in CCD Imager with Lateral Overflow-Gate Shutter." IEEE Transactions on Electron Devices 38 (5): 960. doi:10.1109/16.78365.

Ansper A and Alikas K 2019. "Retrieval of Chlorophyll a from Sentinel-2 MSI Data for the European Union Water Framework Directive Reporting Purposes." Remote Sensing 11 (1): 64. doi:10.3390/rs11010064.

Barbato G, Barini EM, Genta G, and Levi R 2011. "Features and Performance of Some Outlier Detection Methods." Journal of Applied Statistics 38 (10): 2133. doi:10.1080/02664763.2010.545119.

Barker JL 1984. "Relative Radiometric Calibration of Landsat TM Reflective Bands." In: LANDSAT-4 Science Investigations Summary, Greenbelt, MD.

Bodenstorfer E, Fürtler J, Brodersen J, Mayer KJ, Eckel C, Gravogl K, and Nachtnebel H 2007. "High-Speed Line-Scan Camera with Digital Time Delay Integration." In: Real-Time Image Processing 2007, International Society for Optics and Photonics, 64960I.

Bouali M and Ladjal S 2011. "Toward Optimal Destriping of MODIS Data Using a Unidirectional Variational Model." IEEE Transactions on Geoscience and Remote Sensing 49 (8): 2924. doi:10.1109/TGRS.2011.2119399.

Brezonik PL, Olmanson LG, Finlay JC, and Bauer ME 2015. "Factors Affecting the Measurement of CDOM by Remote Sensing of Optically Complex Inland Waters." Remote Sensing of Environment 157: 199. doi:10.1016/j.rse.2014.04.033.

Catano PS 1978. "Blooming in a Charge-Coupled Device Imager. Blooming Control Recommendations are Given for Low-Light-Level CCD Imagers with Time Delay and Integration, Such as the LOPATCH Sensor." Technical Report. San Diego, CA: Naval Ocean Systems Center.

Chamberlain SG and Washkurak WD 1990. "High-Speed, Low-Noise, Fine-Resolution TDI CCD Imagers." In: Charge-Coupled Devices and Solid State Optical Sensors, International Society for Optics and Photonics, 252.

Chissom BS 1970. "Interpretation of the Kurtosis Statistic." The American Statistician 24: 19. doi:10.1080/00031305.1970.10477202.

Clark JM, Schaeffer BA, Darling JA, Urquhart EA, Johnston JM, Ignatius AR, Myer MH, Loftin KA, Werdell PJ, and Stumpf RP 2017. "Satellite Monitoring of Cyanobacterial Harmful Algal Bloom Frequency in Recreational Waters and Drinking Water Sources." Ecological Indicators 80: 84. doi:10.1016/j.ecolind.2017.04.046. [PubMed: 30245589]

Coffer MM, Schaeffer BA, Zimmerman RC, Hill V, Li J, Islam KA, and Whitman PJ 2020. "Performance Across WorldView-2 and RapidEye for Reproducible Seagrass Mapping." Remote Sensing of Environment 250: 112036. doi:10.1016/j.rse.2020.112036. [PubMed: 34334824]

Dai C and Howat IM 2018. "Detection of Saturation in High-Resolution Pushbroom Satellite Imagery." IEEE Journal of Selected Topics in Applied Earth Observations and Remote Sensing 11 (5): 1684. doi:10.1109/JSTARS.2018.2814543.

De Carolis G, Adamo M, and Pasquariello G 2013. "On the Estimation of Thickness of Marine Oil Slicks from Sun-Glittered, Near-Infrared MERIS and MODIS Imagery: The Lebanon Oil Spill Case Study." IEEE Transactions on Geoscience and Remote Sensing 52 (1): 559. doi:10.1109/TGRS.2013.2242476.

Dekker AG and Hestir EL 2012. Evaluating the Feasibility of Systematic Inland Water Quality Monitoring with Satellite Remote Sensing. Canberra, Australia: Commonwealth Scientific and Industrial Research Organization.

Dekker AG, Phinn SR, Anstee J, Bissett P, Brando VE, Casey B, Fearns P, Hedley J, Klonowski W, and Lee ZP 2011. "Intercomparison of Shallow Water Bathymetry, Hydro-optics, and Benthos Mapping Techniques in Australian and Caribbean Coastal Environments." Limnology and Oceanography: Methods 9: 396.

Dogliotti AI, Ruddick KG, Nechad B, Doxaran D, and Knaeps E 2015. "A Single Algorithm to Retrieve Turbidity from Remotely-Sensed Data in All Coastal and Estuarine Waters." Remote Sensing of Environment 156: 157. doi:10.1016/j.rse.2014.09.020.

El Saadi AM, Yousry MM, and Jahin HS 2014. "Statistical Estimation of Rosetta Branch Water Quality Using Multi-Spectral Data." Water Science 28 (1): 18. doi:10.1016/j.wsj.2014.10.001.

El-Desouki MM and Al-Azem B 2014. "Novel CMOS Time-Delay Integration Using Single-Photon Counting for High-Speed Industrial and Aerospace Applications." In: Image Sensors and Imaging Systems 2014, International Society for Optics and Photonics, 902204.

Elvidge CD, Imhoff ML, Baugh KE, Hobson VR, Nelson I, Safran J, Dietz JB, and Tuttle BT 2001. "Night-Time Lights of the World: 1994–1995." ISPRS Journal of Photogrammetry and Remote Sensing 56 (2): 81. doi:10.1016/S0924-2716(01)00040-5.

ESRI. 2019. ArcGIS Desktop: Release 10.7.1.

Gordon HR and Clark DK 1981. "Clear Water Radiances for Atmospheric Correction of Coastal Zone Color Scanner Imagery." Applied Optics 20 (24): 4175. doi:10.1364/AO.20.004175. [PubMed: 20372349]

Gorelick N, Hancher M, Dixon M, Ilyushchenko S, Thau D, and Moore R 2017. "Google Earth Engine: Planetary-Scale Geospatial Analysis for Everyone." Remote Sensing of Environment 202: 18. doi:10.1016/j.rse.2017.06.031.

Gower J, King S, Borstad G, and Brown L 2005. "Detection of Intense Plankton Blooms Using the 709 nm Band of the MERIS Imaging Spectrometer." International Journal of Remote Sensing 26 (9): 2005. doi:10.1080/01431160500075857.

Greb S, Dekker AG, Binding C, Bernard S, Brockmann C, DiGiacomo P, Griffith D, Groom S, Hestir E, and Hunter P 2018. Earth Observations in Support of Global Water Quality Monitoring. Dartmouth, Canada: International Ocean-Colour Coordinating Group.

Hamasaki M, Suzuki T, Kagawa Y, Ishikawa K, Miyata K, and Kambe H 1988. "An IT-CCD Imager with Electronically Variable Shutter Speed. the N-Type Substrate Works as the Shutter-Drain." ITEJ Tech. Rep. Japan 12: 31.

Hansson M and Hakansson B 2007. "The Baltic Algae Watch System-a Remote Sensing Application for Monitoring Cyanobacterial Blooms in the Baltic Sea." Journal of Applied Remote Sensing 1 (1): 11507. doi:10.1117/1.2834769.

Helder DL, Quirk BK, and Hood JJ 1992. "A Technique for the Reduction of Banding in Landsat Thematic Mapper Images." Photogrammetric Engineering & Remote Sensing 58: 1425.

Hestir EL, Brando VE, Bresciani M, Giardino C, Matta E, Villa P, and Dekker AG 2015. "Measuring Freshwater Aquatic Ecosystems: The Need for a Hyperspectral Global Mapping Satellite Mission." Remote Sensing of Environment 167: 181. doi:10.1016/j.rse.2015.05.023.

Hu BL, Hao SJ, Sun DX, and Liu YN 2017. "A Novel Scene-Based Non-Uniformity Correction Method for SWIR Push-Broom Hyperspectral Sensors." ISPRS Journal of Photogrammetry and Remote Sensing 131: 160. doi:10.1016/j.isprsjprs.2017.08.004.

Islam KA, Hill V, Schaeffer B, Zimmerman R, and Li J 2020. "Semi-Supervised Adversarial Domain Adaptation for Seagrass Detection Using Multispectral Images in Coastal Areas." Data Science and Engineering 5 (2): 111. doi:10.1007/s41019-020-00126-0. [PubMed: 32685664]

Kolmogorov A 1933. "Sulla Determinazione Empirica di Una Lgge di Distribuzione." Inst. Ital. Attuari, Giorn 4: 83.

Kolokoussis P and Karathanassi V 2018. "Oil Spill Detection and Mapping Using Sentinel 2 Imagery." Journal of Marine Science and Engineering 6 (1): 4. doi:10.3390/jmse6010004.

Krause KS 2008. "WorldView-1 Pre and Post-Launch Radiometric Calibration and Early on-Orbit Characterization." In: Earth Observing Systems XIII, International Society for Optics and Photonics, 708116.

Kuester M 2017. "Absolute Radiometric Calibration: 2016v0." Technical Report. DigitalGlobe.

Lantz B 2013. "The Large Sample Size Fallacy." Scandinavian Journal of Caring Sciences 27 (2): 487. doi:10.1111/j.1471-6712.2012.01052.x. [PubMed: 22862286]

Lee Z, Hu C, Arnone R, and Liu Z 2012. "Impact of Sub-Pixel Variations on Ocean Color Remote Sensing Products." Optics Express 20 (19): 20844. doi:10.1364/OE.20.020844. [PubMed: 23037208]

Lunetta RS, Schaeffer BA, Stumpf RP, Keith D, Jacobs SA, and Murphy MS 2015. "Evaluation of Cyanobacteria Cell Count Detection Derived from MERIS Imagery Across the Eastern USA." Remote Sensing of Environment 157: 24. doi:10.1016/j.rse.2014.06.008.

Maguire J, Cusack C, Ruiz-Villarreal M, Silke J, McElligott D, and Davidson K 2016. "Applied Simulations and Integrated Modelling for the Understanding of Toxic and Harmful Algal Blooms (ASIMUTH): Integrated HAB Forecast Systems for Europe's Atlantic Arc." Harmful Algae 53: 160. doi:10.1016/j.hal.2015.11.006. [PubMed: 28073441]

Mandelbrot BB 1983. The Fractal Geometry of Nature. San Francisco: W.H. Freeman.

Maxar. 2019. "System-Ready Imagery." https://www.digitalglobe.com/resources

Metzler MD and Malila WA 1985. "Characterization and Comparison of Landsat-4 and Landsat-5 Thematic Mapper Data." Photogrammetric Engineering and Remote Sensing 51: 1315.

Meyer D, Dimitriadou E, Hornik K, Weingessel A, and Leisch F 2019. "E1071: Misc Functions of the Department of Statistics, Probability Theory Group (Formerly: E1071), TU Wien." https://cran.r-project.org/package=e1071

Mishra S, Stumpf RP, and Meredith A 2019. "Evaluation of RapidEye Data for Mapping Algal Blooms in Inland Waters." International Journal of Remote Sensing 40 (7): 2811. doi:10.1080/01431161.2018.1533657.

Mouw CB, Greb S, Aurin D, DiGiacomo PM, Lee Z, Twardowski M, Binding C, Hu C, Ma R, and Moore T 2015. "Aquatic Color Radiometry Remote Sensing of Coastal and Inland Waters: Challenges and Recommendations for Future Satellite Missions." Remote Sensing of Environment 160: 15. doi:10.1016/j.rse.2015.02.001.

Nichol JE and Vohora V 2004. "Noise Over Water Surfaces in Landsat TM Images." International Journal of Remote Sensing 25 (11): 2087. doi:10.1080/014311603100001618770.

Odermatt D, Gitelson A, Brando VE, and Schaepman M 2012. "Review of Constituent Retrieval in Optically Deep and Complex Waters from Satellite Imagery." Remote Sensing of Environment 118: 116. doi:10.1016/j.rse.2011.11.013.

Oiry S and Barillé L 2021. "Using Sentinel-2 Satellite Imagery to Develop Microphytobenthos-Based Water Quality Indices in Estuaries." Ecological Indicators 121: 107184. doi:10.1016/j.ecolind.2020.107184.

Olmanson LG, Bauer ME, and Brezonik PL 2008. "A 20-Year Landsat Water Clarity Census of Minnesota's 10,000 Lakes." Remote Sensing of Environment 112 (11): 4086. doi:10.1016/j.rse.2007.12.013.

Pahlevan N, Sarkar S, Franz BA, Balasubramanian SV, and He J 2017a. "Sentinel-2 MultiSpectral Instrument (MSI) Data Processing for Aquatic Science Applications: Demonstrations and Validations." Remote Sensing of Environment 201: 47. doi:10.1016/j.rse.2017.08.033.

Pahlevan N, Schott JR, Franz BA, Zibordi G, Markham B, Bailey S, Schaaf CB, Ondrusek M, Greb S, and Strait CM 2017b. "Landsat 8 Remote Sensing Reflectance (Rrs) Products: Evaluations, Intercomparisons, and Enhancements." Remote Sensing of Environment 190: 289. doi:10.1016/j.rse.2016.12.030.

Palmer SCJ, Kutser T, and Hunter PD 2015. "Remote Sensing of Inland Waters: Challenges, Progress and Future Directions." Remote Sensing of Environment 157: 1. doi:10.1016/j.rse.2014.09.021.

Pancorbo JL, Lamb BT, Quemada M, Hively WD, Gonzalez-Fernandez I, and Molina I 2021. "Sentinel-2 and WorldView-3 Atmospheric Correction and Signal Normalization Based on

Ground-Truth Spectroradiometric Measurements." ISPRS Journal of Photogrammetry and Remote Sensing 173: 166. doi:10.1016/j.isprsjprs.2021.01.009.

Papenfus M, Schaeffer B, Pollard AI, and Loftin K 2020. "Exploring the Potential Value of Satellite Remote Sensing to Monitor Chlorophyll-a for US Lakes and Reservoirs." Environmental Monitoring and Assessment 192 (12): 808. doi:10.1007/s10661-020-08631-5. [PubMed: 33263783]

Pasqualini V, Pergent-Martini C, Pergent G, Agreil M, Skoufas G, Sourbes L, and Tsirika A 2005. "Use of SPOT 5 for Mapping Seagrasses: An Application to Posidonia Oceanica." Remote Sensing of Environment 94 (1): 39. doi:10.1016/j.rse.2004.09.010.

Pirasteh S, Mollaee S, Fatholahi SN, and Li J 2020. "Estimation of Phytoplankton Chlorophyll-a Concentrations in the Western Basin of Lake Erie Using Sentinel-2 and Sentinel-3 Data." Canadian Journal of Remote Sensing 46 (5): 585. doi:10.1080/07038992.2020.1823825.

Poli D, Remondino F, Angiuli E, and Agugiaro G 2015. "Radiometric and Geometric Evaluation of GeoEye-1, WorldView-2 and Pléiades-1A Stereo Images for 3D Information Extraction." ISPRS Journal of Photogrammetry and Remote Sensing 100: 35. doi:10.1016/j.isprsjprs.2014.04.007.

R Core Team. 2020. "R: A Language and Environment for Statistical Computing." https://www.R-project.org/

Rakwatin P, Takeuchi W, and Yasuoka Y 2007. "Stripe Noise Reduction in MODIS Data by Combining Histogram Matching with Facet Filter." IEEE Transactions on Geoscience and Remote Sensing 45 (6): 1844. doi:10.1109/TGRS.2007.895841.

Rosen BH, Davis TW, Gobler CJ, Kramer BJ, Loftin KA, and Survey USG 2017. "Cyanobacteria of the 2016 Lake Okeechobee and Okeechobee Waterway Harmful Algal Bloom." Technical Report. Reston, VA. http://pubs.er.usgs.gov/publication/ofr20171054

Schaeffer B and Myer M 2020. "Resolvable Estuaries for Satellite Derived Water Quality Within the Continental United States." Remote Sensing Letters 11 (6): 535. doi:10.1080/2150704X.2020.1717013.

Seuront L, Schmitt F, Lagadeuc Y, Schertzer D, Lovejoy S, and Frontier S 1996. "Multifractal Analysis of Phytoplankton Biomass and Temperature in the Ocean." Geophysical Research Letters 23 (24): 3591. doi:10.1029/96GL03473.

Smirnov NV 1939. "On the Estimation of the Discrepancy Between Empirical Curves of Distribution for Two Independent Samples." Bull. Math. Univ. Moscou 2: 3.

Smith SL, Mooney JA, Tantalo TA, and Fiete RD 1999. "Understanding Image Quality Losses Due to Smear in High-Resolution Remote Sensing Imaging Systems." Optical Engineering 38 (5): 821. doi:10.1117/1.602054.

Toming K, Kutser T, Laas A, Sepp M, Paavel B, and Nõges T 2016. "First Experiences in Mapping Lake Water Quality Parameters with Sentinel-2 MSI Imagery." Remote Sensing 8 (8): 640. doi:10.3390/rs8080640.

Traganos D and Reinartz P 2017. "Mapping Mediterranean Seagrasses with Sentinel-2 Imagery." Marine Pollution Bulletin 134: 197. doi:10.1016/j.marpolbul.2017.06.075. [PubMed: 28676173]

Updike T and Comp C 2010. "Radiometric Use of WorldView-2 Imagery." Technical Report. DigitalGlobe.

Wahballah WA, Bazan TM, and Ibrahim M 2018. "Smear Effect on High-Resolution Remote Sensing Satellite Image Quality." In: 2018 IEEE Aerospace Conference, IEEE, 1.

Wang X, Gong Z, and Pu R 2018. "Estimation of Chlorophyll a Content in Inland Turbidity Waters Using WorldView-2 Imagery: A Case Study of the Guanting Reservoir, Beijing, China." Environmental Monitoring and Assessment 190 (10): 1. doi:10.1007/s10661-018-6978-7.

Warren MA, Simis SGH, Martinez-Vicente V, Poser K, Bresciani M, Alikas K, Spyrakos E, Giardino C, and Ansper A 2019. "Assessment of Atmospheric Correction Algorithms for the Sentinel-2A MultiSpectral Imager Over Coastal and Inland Waters." Remote Sensing of Environment 225: 267. doi:10.1016/j.rse.2019.03.018.

Wasserstein RL, Schirm AL, and Lazar NA 2019. "Moving to a World Beyond "P < 0.05"." The American Statistician 73: 1. doi:10.1080/00031305.2019.1583913.

Wu T, Qin B, Zhu G, Luo L, Ding Y, and Bian G 2013. "Dynamics of Cyanobacterial Bloom Formation During Short-Term Hydrodynamic Fluctuation in a Large Shallow, Eutrophic, and

Wind-Exposed Lake Taihu, China." Environmental Science and Pollution Research 20 (12): 8546. doi:10.1007/s11356-013-1812-9. [PubMed: 23677755]

Wynne TT, Stumpf R, Tomlinson M, and Dyble J 2010. "Characterizing a Cyanobacterial Bloom in Western Lake Erie Using Satellite Imagery and Meteorological Data." Limnology and Oceanography 55 (5): 2025. doi:10.4319/lo.2010.55.5.2025.

Wynne TT, Stumpf RP, Tomlinson MC, Warner RA, Tester PA, Dyble J, and Fahnenstiel GL 2008. "Relating Spectral Shape to Cyanobacterial Blooms in the Laurentian Great Lakes." International Journal of Remote Sensing 29 (12): 3665. doi:10.1080/01431160802007640.

Xu M, Liu H, Beck R, Lekki J, Yang B, Shu S, Kang EL et al. .2019. "A Spectral Space Partition Guided Ensemble Method for Retrieving Chlorophyll-a Concentration in Inland Waters from Sentinel-2A Satellite Imagery." Journal of Great Lakes Research 45 (3): 454. doi:10.1016/j.jglr.2018.09.002.

Zhang Y, Zhang Y, Shi K, Zhou Y, and Li N 2021. "Remote Sensing Estimation of Water Clarity for Various Lakes in China." Water Research 192: 116844. doi:10.1016/j.watres.2021.116844. [PubMed: 33494039]

Zhao Y, Pu R, Bell SS, Meyer C, Baggett LP, and Geng X 2013. "Hyperion Image Optimization in Coastal Waters." IEEE Transactions on Geoscience and Remote Sensing 51 (2): 1025. doi:10.1109/TGRS.2012.2205262.

Highlights

- Banding and striping were identified in WorldView-3 imagery of an aquatic system

- Striping caused inconsistent, erroneous values for a derived bio-geophysical variable

- All spectral bands had banding caused by detector sub-array non-uniformity

- The red, NIR #1 spectral bands had striping caused by image acquisition parameters

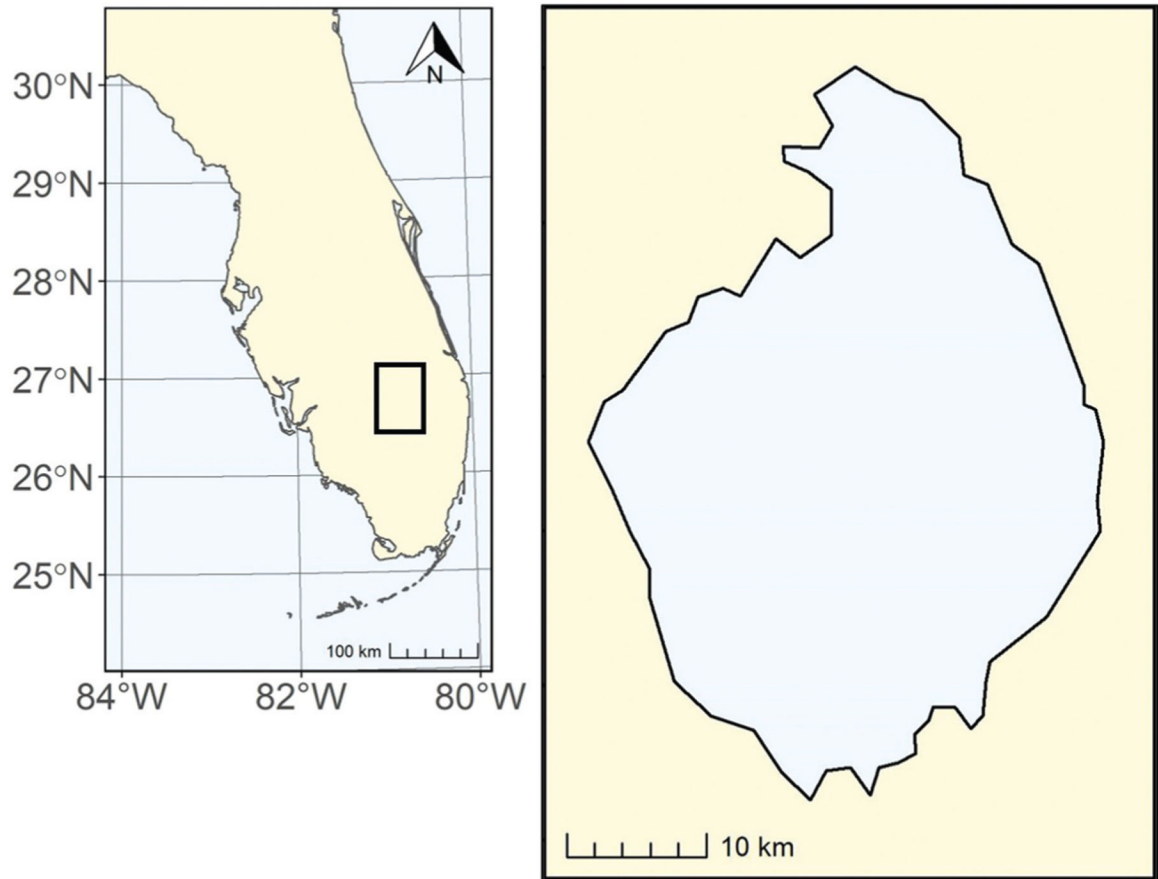- Default acquisition parameters are set for land, revising for water eased striping

Figure 1.
Lake Okeechobee is located in southeastern Florida (26.97°N, 80.80°W), USA, and is the largest lake in the state and the fifth largest lake in the country by surface area, excluding the Great Lakes.
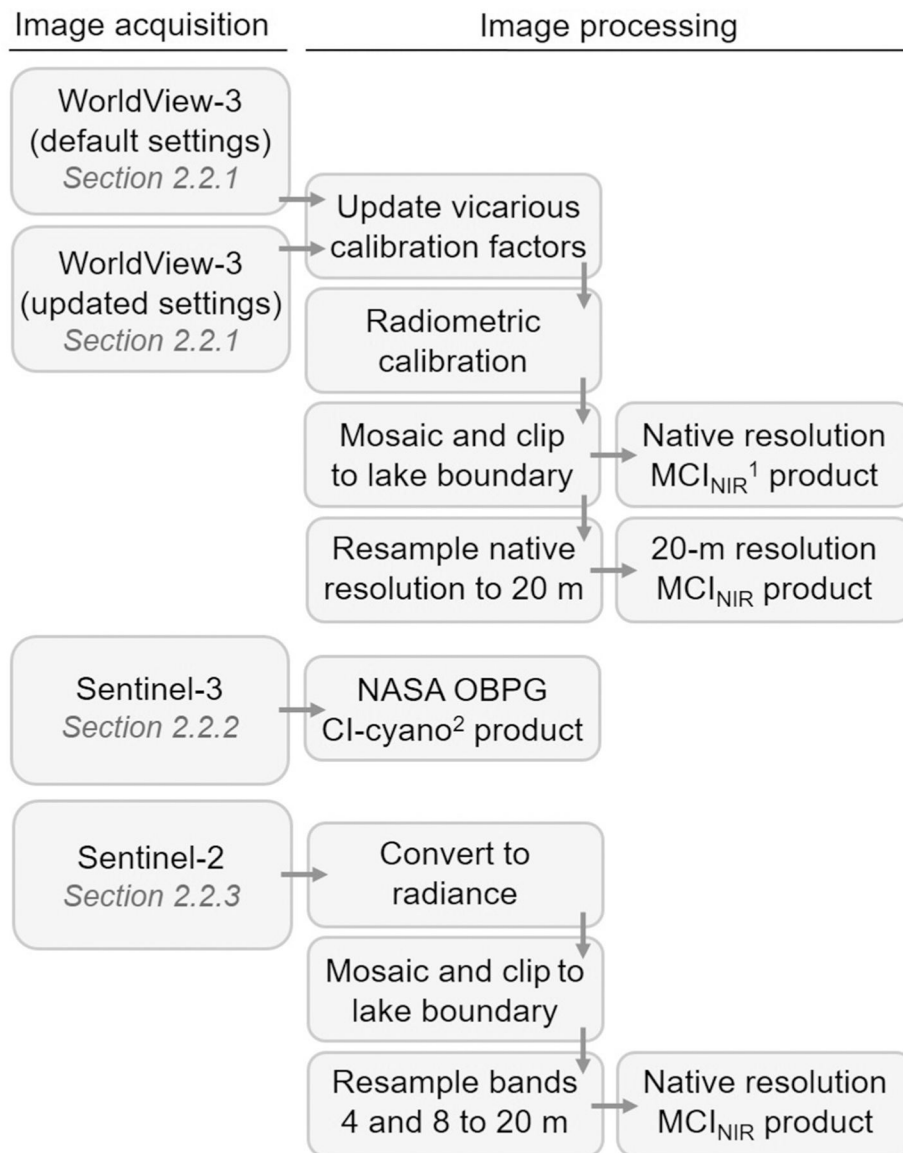
Figure 2.
A flowchart outlining specific image processing steps applied to WorldView-3 (Section 2.2.1), Sentinel-3 (Section 2.2.2), and Sentinel-2 (Section 2.2.3) imagery. [1]Near-infrared (NIR) maximum chlorophyll index (MCI_{NIR}) [2]National Aeronautics and Space Administration (NASA) Ocean Biology Processing Group (OBPG) cyanobacteria index product (CI-cyano) retrieved from https://oceancolor.gsfc.nasa.gov/projects/cyan/
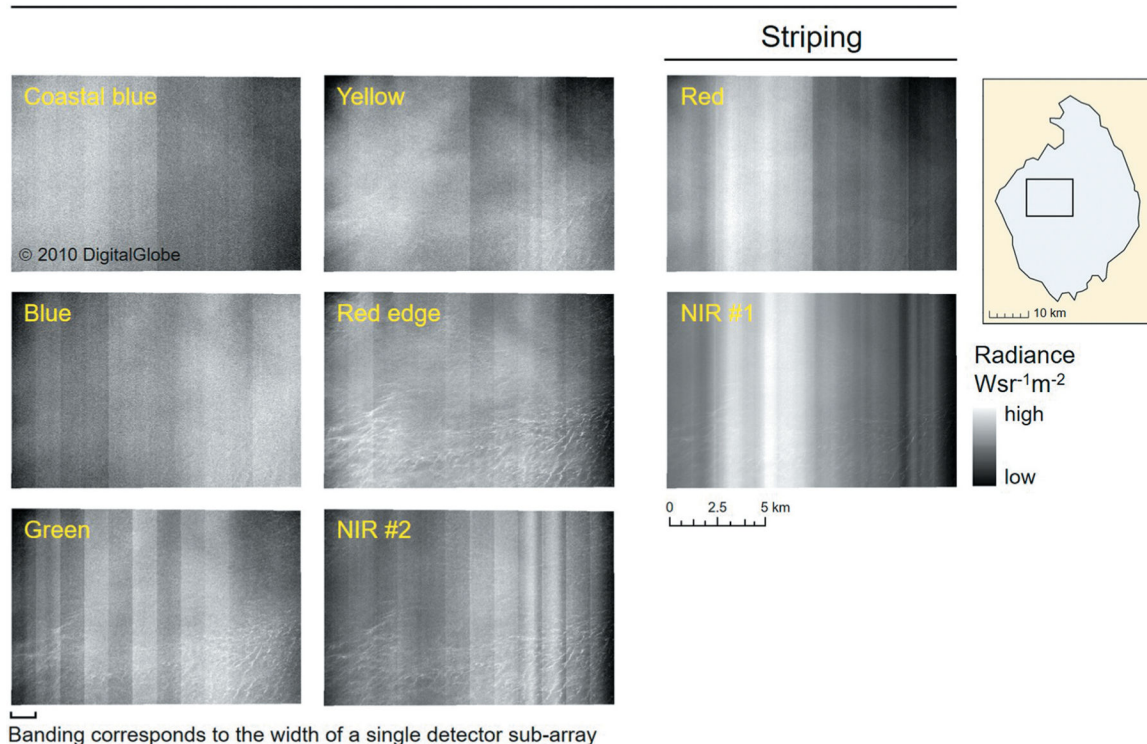
Figure 3.
Radiance measured by each WorldView-3 spectral band for a single tile at Lake
Okeechobee, Florida, on 30 August 2017. Vertical artefacts called banding appear in all
eight spectral bands and correspond to the 12 multispectral detector sub-arrays that make
up the WorldView-2 and WorldView-3 focal planes. Vertical artefacts called striping appear
in two of the eight spectral bands. Note: the radiance scale is stretched for each individual
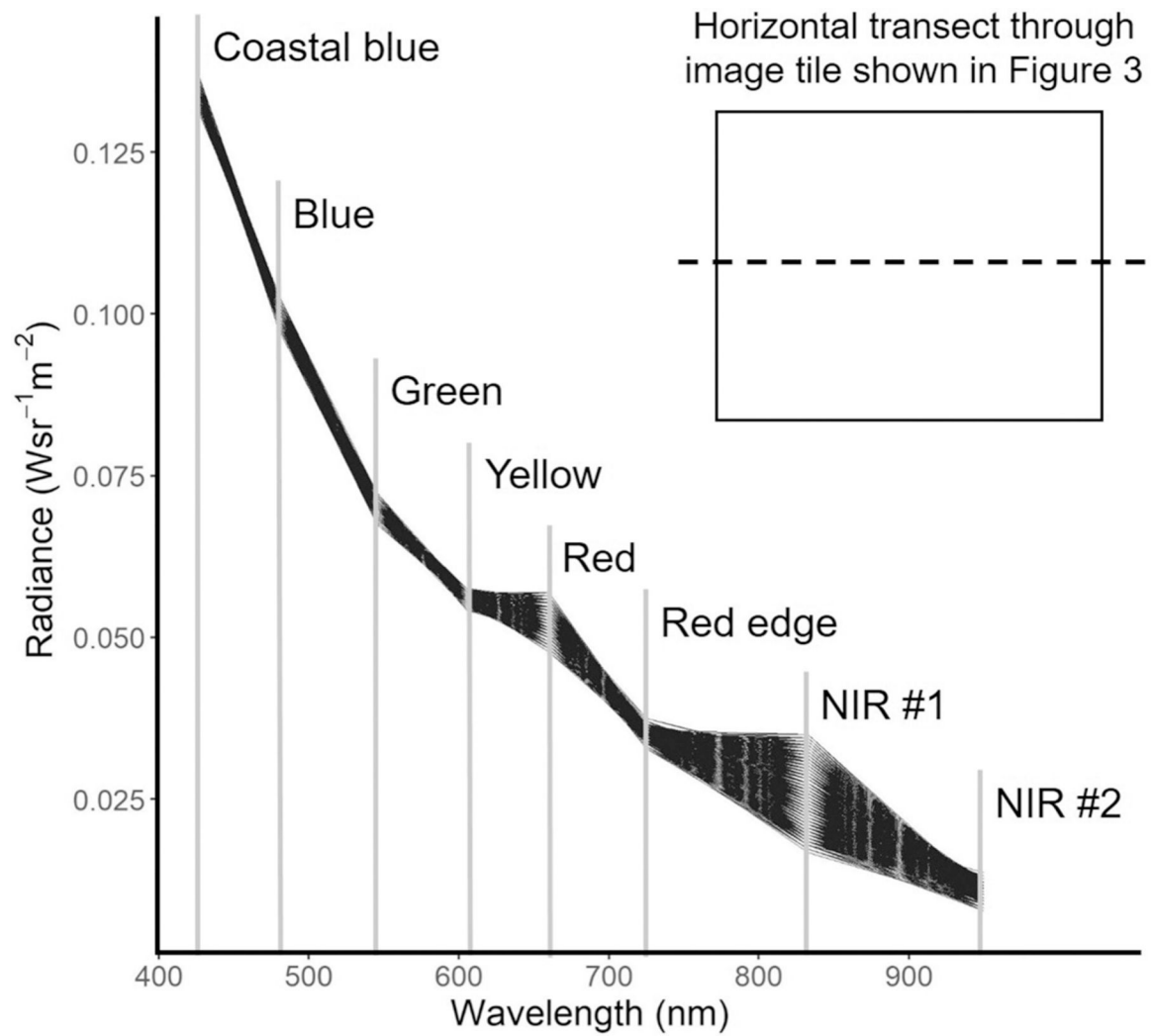spectral band to optimize visualization.

Figure 4.
Radiance values extracted for all pixels (n = 12,548) across a horizontal transect for the
WorldView-3 image tile shown in Figure 3.
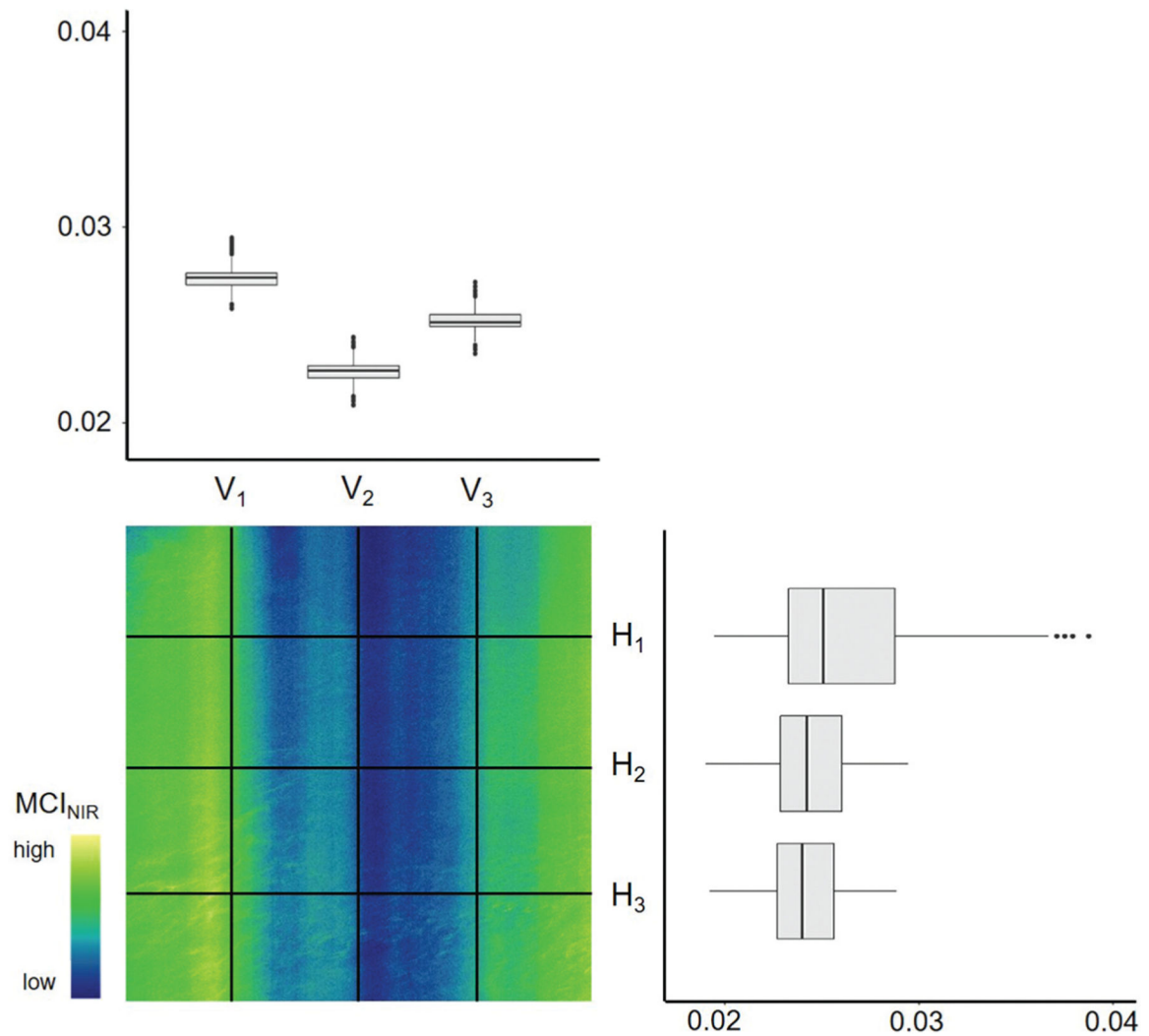
Figure 5.
The near-infrared (NIR) maximum chlorophyll index (MCI$_{NIR}$) for a spatial subset of the image tile shown in Figure 3 at Lake Okeechobee, Floria, on 30 August 2017 derived using imagery from WorldView-3. Boxplots describing the distribution of MCI$_{NIR}$ data values for three vertical transects are shown above the raster image and for three horizontal transects to the right of the raster image. Gray boxes represents the 25th percentile, median, and 75th percentile; the lower whisker extends to 1.5 times the interquartile range from the 25th percentile; the top whisker extends to 1.5 times the interquartile range from the 75th percentile; black dots represent outliers that fall outside these ranges.
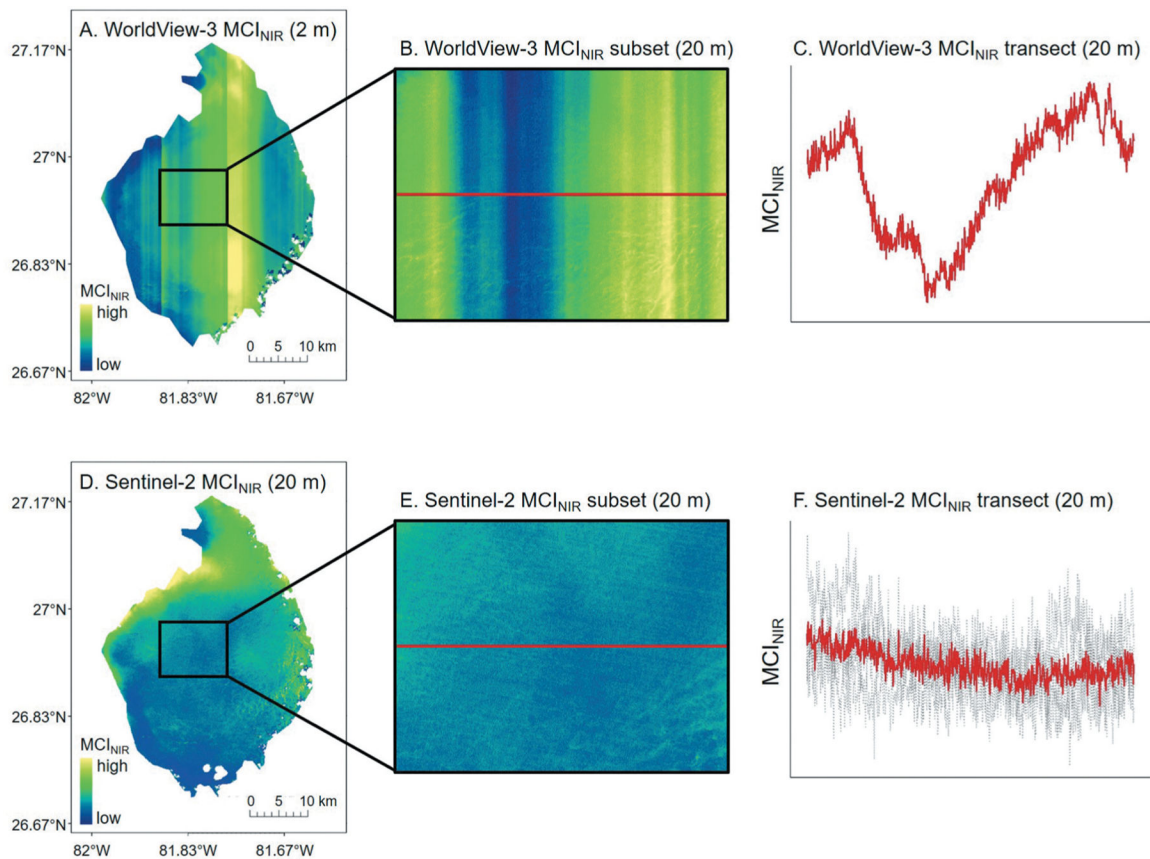
Figure 6.
(a) The near-infrared (NIR) maximum chlorophyll index (MCI$_{NIR}$) at Lake Okeechobee, Florida, from WorldView-3 imagery collected on 30 August 2017 at a spatial resolution of approximately 2 m. (b) A spatial subset of (a) resampled to match the 20-m spatial resolution of Sentinel-2. (c) A horizontal transect of MCI$_{NIR}$ corresponding to the red line in (b). (d) A composite average of MCI$_{NIR}$ for Lake Okeechobee generated using four Sentinel-2 scenes collected in August and September 2017. (e) A spatial subset of (d). (f) A horizontal transect of MCI$_{NIR}$ corresponding to the red line in (e), including the composite MCI$_{NIR}$ values (red line) and the MCI$_{NIR}$ values for the four scenes used to generate the composite (gray lines). Note: Radiance measured by WorldView-3 and Sentinel-2 have not been cross-calibrated; thus, the resulting MCI$_{NIR}$ values derived from each sensor cannot be directly compared and the extracted data do not use the same quantitative scales.
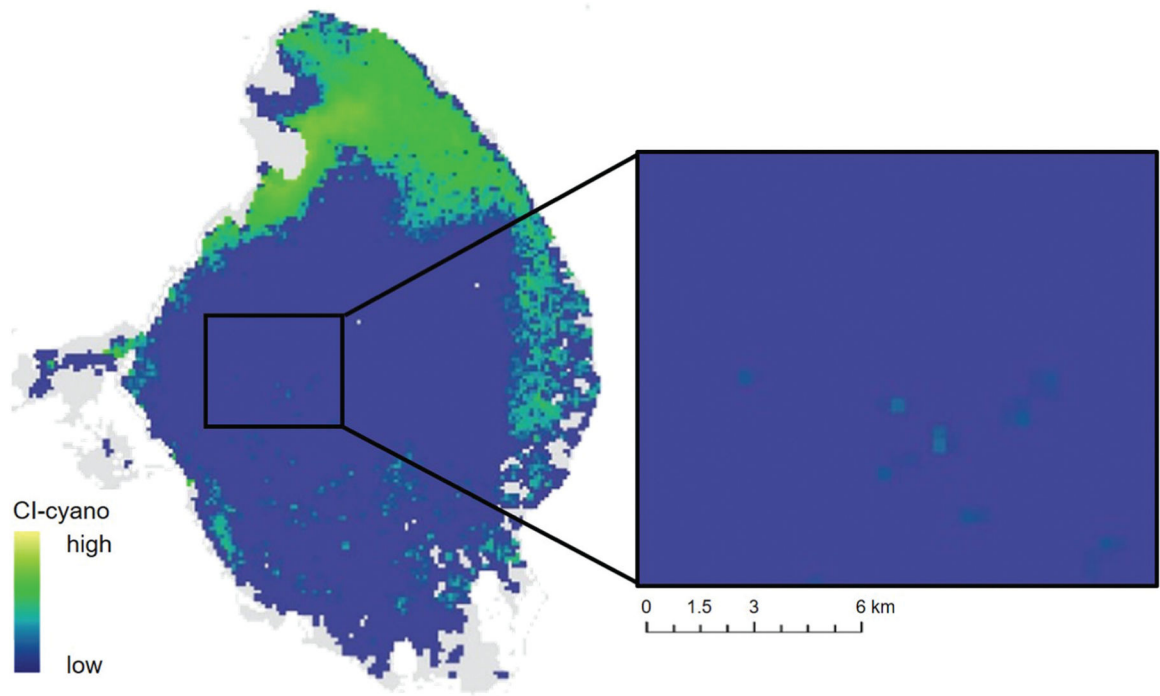
Figure 7.
Cyanobacteria abundance estimated from the cyanobacteria index (CI-cyano) for Sentinel-3 imagery collected at Lake Okeechobee, Florida, on 31 August 2017, one day after a WorldView-3 image acquisition.
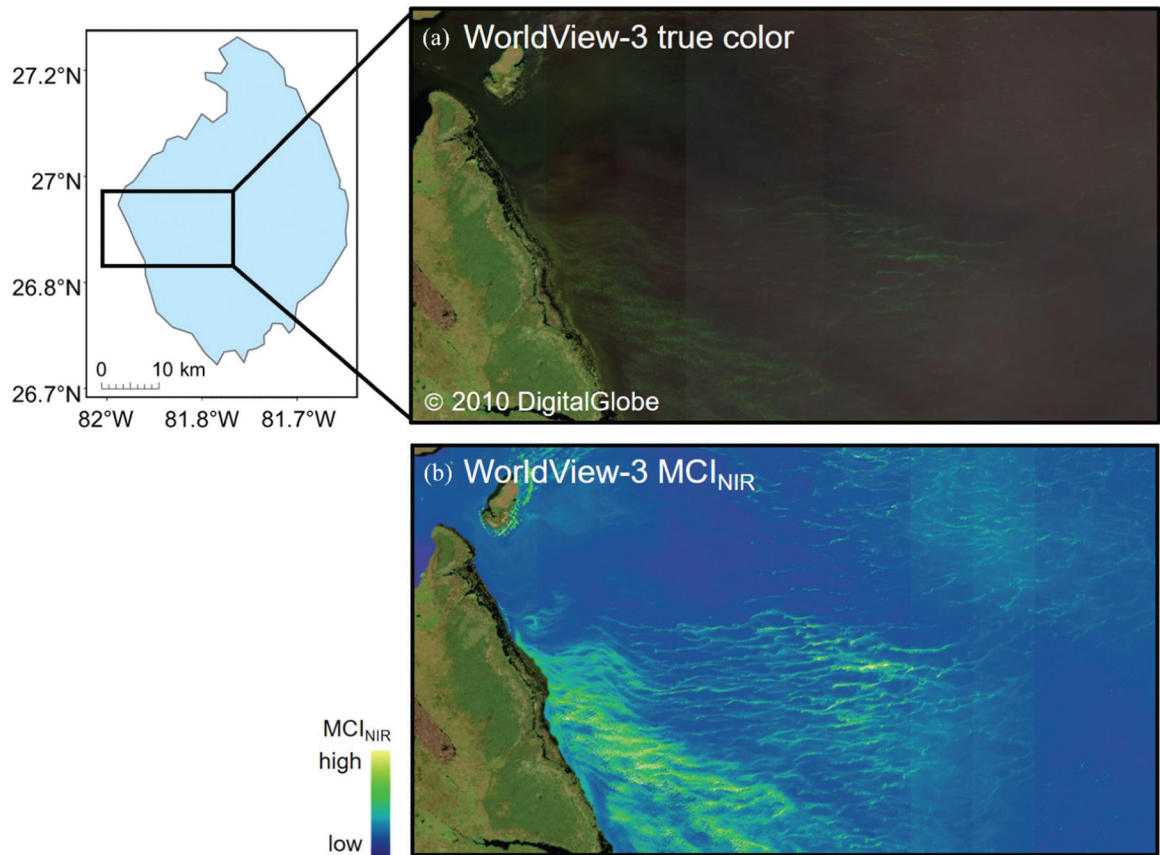
Figure 8.
WorldView-3 (a) true color image and (b) near-infrared (NIR) maximum chlorophyll index
(MCI_{NIR}) for a spatial subset of Lake Okeechobee, Florida, on 26 May 2021.
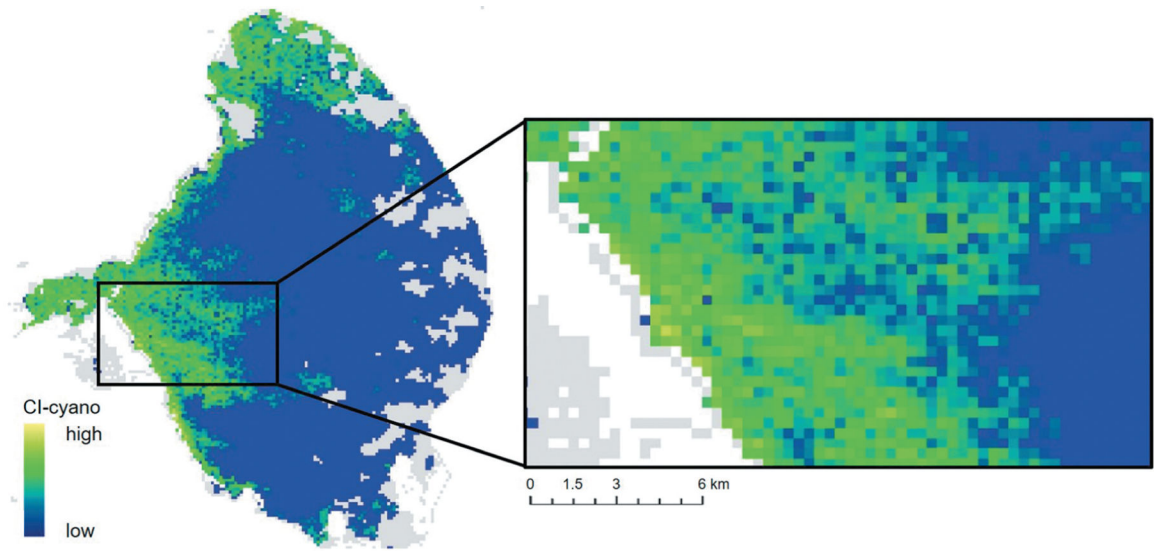
Figure 9.
Cyanobacteria abundance estimated from the cyanobacteria index (CI-cyano) for Sentinel-3 imagery collected at Lake Okeechobee, Florida, on 26 May 2021, coinciding with a WorldView-3 image acquisition.
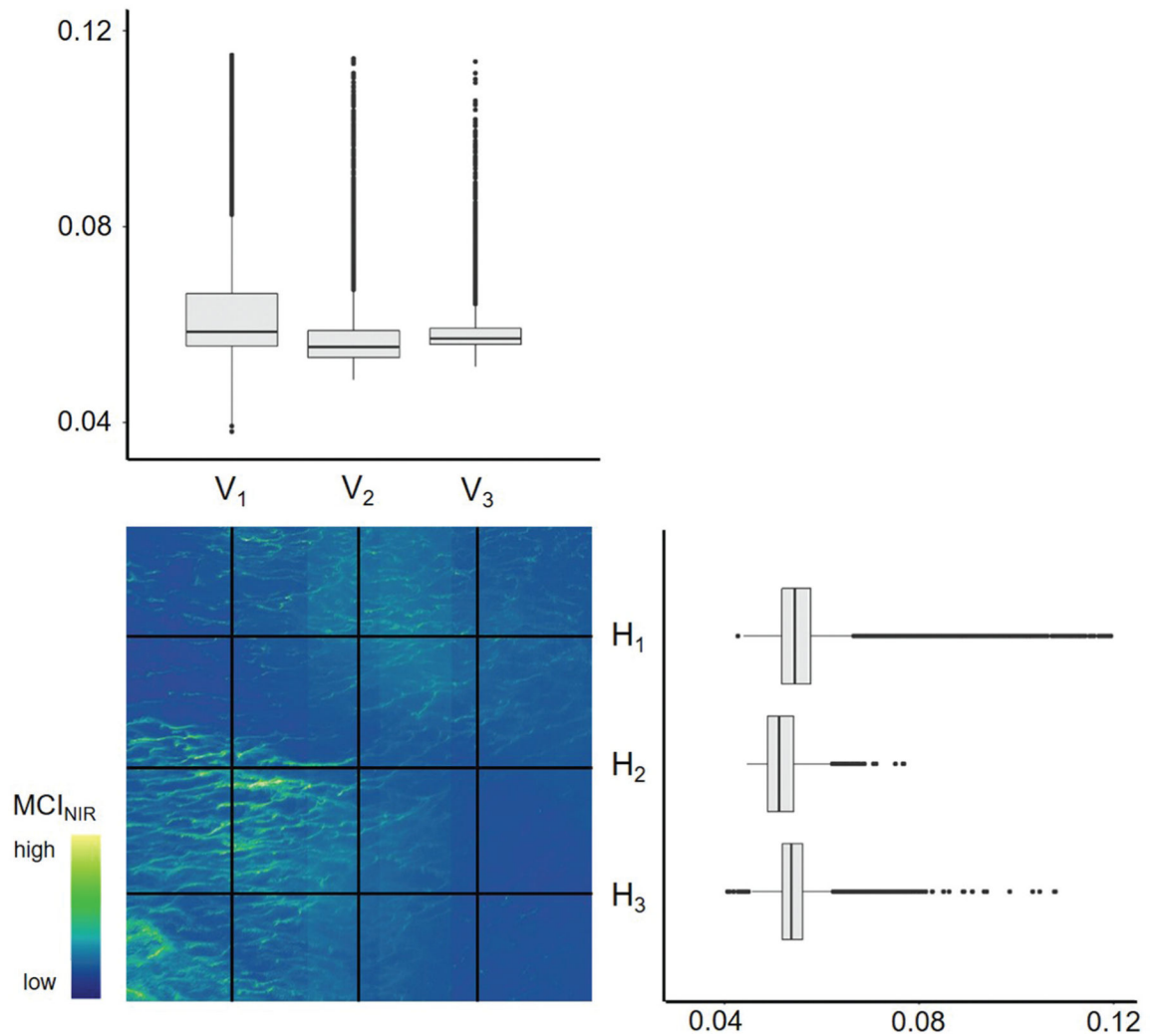
Figure 10.
The near-infrared (NIR) maximum chlorophyll index (MCI_{NIR}) for a spatial subset of the image tile shown in Figure 3 at Lake Okeechobee, Florida, on 26 May 2021 derived using imagery from WorldView-3. Boxplots describing the distribution of MCI_{NIR} data values for three vertical transects are shown above the raster image and boxplots describing the distribution of MCI_{NIR} data values for three horizontal transects are shown to the right of the raster image. Gray boxes represents the 25th percentile, median, and 75th percentile; the lower whisker extends to 1.5 times the interquartile range from the 25th percentile; the top whisker extends to 1.5 times the interquartile range from the 75th percentile; black dots represent outliers that fall outside these ranges.

Table 1.

Acquisition dates for images collected from WorldView-3, Sentinel-3, and Sentinel-2.

Satellite	Image acquisition date
WorldView-3	30 August 2017
	26 May 2021
Sentinel-3	31 August 2017
	26 May 2021
Sentinel-2	4 August 2017
	19 August 2017
	13 September 2017
	28 September 2017

Table 2.

WorldView-3 and Sentinel-2 centre wavelengths (nm) for the three spectral bands used to compute the near-infrared (NIR) maximum chlorophyll index (MCI_{NIR}) originally defined as MCI by Gower et al. (2005).

Spectral band	WorldView-3	Sentinel-2
Red	661	665
Red edge	724	704
NIR	832	842

Table 3.

Average (μ) and standard deviation (σ) of radiance values accompanying the spectra extracted from all pixels (n = 12,548) across the horizontal transect shown in Figure 4. Mild and extreme outliers were defined by Barbato et al. (2011).

Spectral band	μ	σ
Coastal blue	0.1351	0.0009
Blue	0.1007	0.0008
Green	0.0703	0.0008
Yellow	0.0562	0.0005
Red	0.0528	0.0020 [*]
Red edge	0.0351	0.0005
NIR #1	0.0259	0.0048 [**]
NIR #2	0.0106	0.0009

[*] mild outlier ($\sigma > 0.0014$)

[**] extreme outlier ($\sigma > 0.0021$)

Table 4.

Results of the two-sample Kolmogorov–Smirnov test for a WorldView-3 image collected at Lake Okeechobee, Florida, on 31 August 2017; the sample size for each sample was 8477. D is the Kolmogorov–Smirnov test statistic. V_1, V_2, and V_3 represent the three vertical transects shown in Figure 5, and H_1, H_2, and H_3 represent the three horizontal transects.

Sample A	Sample B	D	Difference
V_1	V_2	1.00	Large
V_1	V_3	0.99	Large
V_2	V_3	1.00	Large
H_1	H_2	0.07	Small
H_1	H_3	0.37	Small
H_2	H_3	0.34	Small

Table 5.

Results of the two-sample Kolmogorov–Smirnov test for a WorldView-3 image collected at Lake Okeechobee, Florida, on 26 May 2021; the sample size for each sample was 9035. D is the Kolmogorov–Smirnov test statistic. V_1, V_2, and V_3 represent the three vertical transects shown in Figure 10, and H_1, H_2, and H_3 represent the three horizontal transects.

Sample A	Sample B	D	Difference
V_1	V_2	0.33	Small
V_1	V_3	0.12	Small
V_2	V_3	0.30	Small
H_1	H_2	0.30	Small
H_1	H_3	0.26	Small
H_2	H_3	0.36	Small